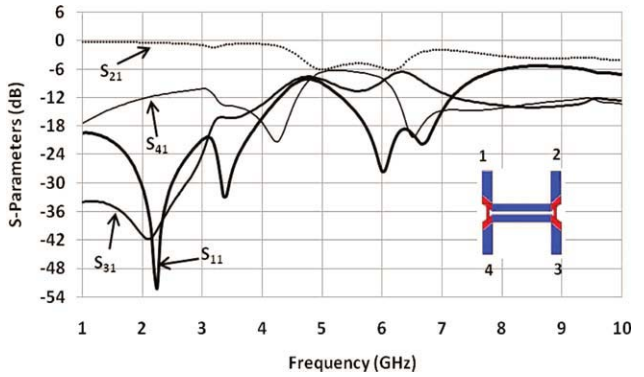

Figure 11 The simulated S-parameters for the DGS microstrip directional coupler when $L_2 = 3.0$ mm. [Color figure can be viewed in the online issue, which is available at www.interscience.wiley.com]

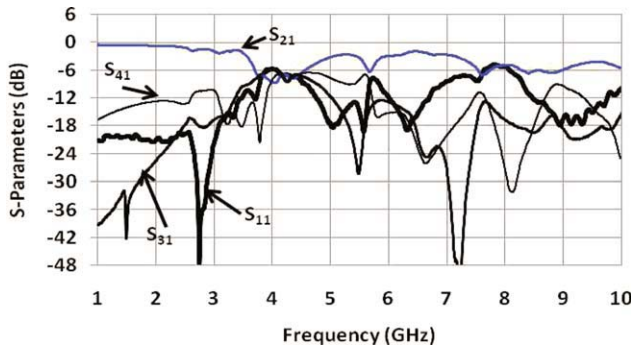

Figure 12 The Measured S-parameters for the DGS microstrip directional coupler when $L_2 = 3.0$ mm. [Color figure can be viewed in the online issue, which is available at www.interscience.wiley.com]

ACKNOWLEDGMENTS

The authors would like to acknowledge the assistance and the financial support for this work that provided by the Research Center, College of Engineering at King Saud University.

REFERENCES

1. S.B. Cohn and R. Levy, History of microwave passive components with particular attention to directional couplers, IEEE Trans Microwave Theory Tech 32 (1984), 1046–1054.
2. E.M.T. Hones and J.T. Bolljahn, Coupled-strip-transmission-line filters and directional couplers, IRE Trans Microwave Theory Tech 4 (1956), 75–81.
3. S.B. Cohn, Parallel-coupled transmission line resonators, IRE Trans Microwave Theory Tech 6 (1958), 223–231.
4. G.L. Matthaei, Interdigital bandpass filters, IRE Trans Microwave Theory Tech 10 (1962), 479–491.
5. R. Levy, General synthesis of asymmetric multi-element coupled transmission line directional couplers, IEEE Trans Microwave Theory Tech 11 (1963), 227–231.
6. G.I. Zysman and A.K. Johnson, Coupled transmission line networks in an inhomogeneous dielectric medium, IEEE Trans Microwave Theory Tech 17 (1969), 753–759.
7. E.G. Cristal, Coupled-transmission-Line directional couplers with coupled lines of unequal characteristic impedances, IEEE Trans Microwave Theory Tech 14 (1966), 337–346.
8. J.P. Shelton, Impedances of offset parallel-coupled strip transmission lines, IEEE Trans Microwave Theory Tech 14 (1966), 7–15.
9. J.P. Shelton and J.A. Mosko, Synthesis and design of wideband equal ripple TEM directional couplers and fixed phase shifters, IEEE Trans Microwave Theory Tech 14 (1966), 462–473.
10. M.J. Park and B. Lee Compact foldable coupled-line cascade couplers, IEE Proc Microwave Antennas Propag 153 (2006), 237–240.
11. L.G. Maloratsky, Passive RF & Microwave Integrated Circuits, Newnes, 2004, pp. 117–162.
12. M. Caulton, B. Hershenov, S.P. Knight, and R.E. Debrecht, Status of lumped elements in microwave integrated circuit-present and future, IEEE Trans Microwave Theory Tech 19 (1971), 588–599.
13. J. Post, An exact lumped-element equivalent circuit model for transmission-line transformers formed from coupled microstrip lines, Microwave Opt technol lett 49 (2007), 2984–2988.
14. T.N. Kuo, Y.S. Lin, C.H. Wang, and C.H. Chen, A compact LTCC branch-line coupler using modified-T equivalent-circuit model for transmission line, IEEE Microwave Wireless Compon Lett 16 (2006), 90–92.
15. C.-S. Kim, J.-S. Park, D. Ahn, and J.-B. Lim, A Novel 1-D Periodic Defected Ground Structure for Planar Circuits, IEEE Microwave Guid Wave Lett 10 (2000), 131–133.
16. D. Ahn, J.S. Park, C.S. Kim, J. Kim, Y. Qian, and T. Itoh, A design of the low pass filter using novel microstrip defected ground structures, IEEE Trans Microwave Theory Tech 49 (2001), 86–92.
17. H.-W. Liu, Z.-F. Li, X.-W. Sun, and J.-F. Mao, An Improved 1-D Periodic Defected Ground Structure for Microstrip Line, IEEE Microwave Wireless compon Lett 14 (2004), 180–182.
18. J.-S. Hong and B.M Karyamapudi, A General Circuit Model for Defected Ground Structures in Planar Transmission Lines, IEEE Microwave Wireless compon Lett 15 (2005), 706–708.
19. S.K. Parui and S. Das, Simple Defected Ground Structure with Elliptical Lowpass filtering Response, Proceedings of Asia-Pacific Microwave Conference, Bangkok, Thailand, 2007.
20. J. Yang and W. Wu, Compact Elliptic-Function Low-Pass Filter Using Defected Ground Structure, IEEE Microwave Wireless compon Lett 18 (2008), 578–580.
21. A.S. Mohra, Compact Lowpass Filter with Sharp Transition Band Based on Defected Ground Structures, Prog Electromagnetics Res Lett 8 (2009), 83–92.

EXPERIMENTAL OBSERVATION OF PHOTO-EXCITED ELECTRON DEPLETION FOR STABILITY IMPROVEMENT IN A LITHIUM NIOBATE POLARIZATION CONVERTER

Ruey-Ching Twu,[1] Hsuan-Hsien Lee,[2] and Hao-Yang Hong[1]

[1] Department of Electro-Optical Engineering, Southern Taiwan University, Tainan 710, Taiwan; Corresponding author: rctwu@mail.stut.edu.tw

[2] Department of Electrical Engineering, Southern Taiwan University, Tainan 710, Taiwan

Received 26 November 2009

ABSTRACT: *The relations between conversion stabilities and photo-excited electron-depletion effects have been experimentally evaluated in a Zn-indiffused lithium niobate polarization converter, for the first time. A simple method with a biased voltage and laser trimming was performed to observe these phenomena. The results show that the stable conversions for both polarities of applied polarization-conversion voltages are achievable due to the depletion of photo-excited electrons in the waveguides.* © 2010 Wiley Periodicals, Inc. Microwave Opt Technol Lett 52: 1937–1941, 2010; Published online in Wiley InterScience (www.interscience.wiley.com). DOI 10.1002/mop.25384

Key words: *polarization converter; lithium niobate; photorefractive*

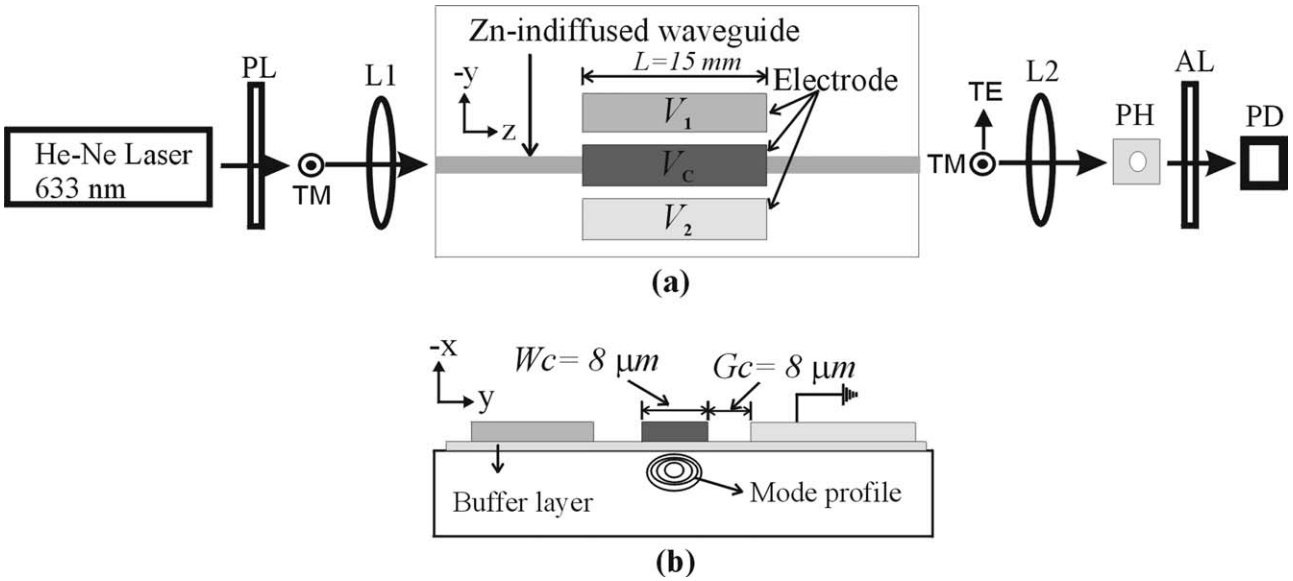

Figure 1 (a) Measurement setup and (b) device structure of the ZIPC

1. INTRODUCTION

Photorefractive effects are essential issues in the development of lithium niobate (LN) optical waveguide devices. Because the photoexcitable electrons can be released under the high irradiating powers of the visible lights, the spatially nonuniform distributions of electrons easily build up a space-charge electric field [1]. Then, the refractive index changes in the channel waveguides through an elelctrooptic (EO) effect. The changes of optical phase conditions easily cause the conversion wavelength shifts of nonlinear optic devices and unstable bias operations of EO phase modulators [2–4]. Consequently, the suppression of photorefraction in LN is of great importance for improving device performance. Similar to the buck-type EO wave plates for controlling the states of polarization [5], the waveguide-type LN polarization controllers have the advantages of compact size and low driving voltage [6]. However, most of the reported *x*-cut/*z*-propagation Ti-indiffused (TI) polarization converters are used in the infrared wavelengths [7], which are difficult to be used in the visible wavelengths due to photorefractive effects [8]. To obtain a compact LN polarization controller for the visible wavelengths, stable polarization converters are necessary components. In comparison with the TI waveguide devices, the Zn-indifussed (ZI) waveguide devices have better phase stabilities due to less photorefractive effects [9, 10].

In this article, we explore the relations between conversion stabilities and the photo-excited electron-depletion effects in the ZI polarization converter (ZIPC) by using the treatments of biased voltage and laser trimming at room temperature. After treatments, the polarization conversions became stable due to the depletion of the photo-excited electrons in the channel waveguides. Although the applied voltages for complete conversion are increased from 5 to 8 V after treatments, the electron-depletion effects to suppress the phase-bias drift are still worthwhile evaluations for improving the stability of the ZIPC.

2. DEVICE PRINCIPLES AND MEASUREMENTS

Figure 1 displays the measurement setup and device structure of the ZIPC. The ZIPC is same as discussed in a previous report [4]. It consists of a channel waveguide of 4 μm-wide and 22 mm-long with three parallel aluminum electrodes of 300 nm, which was formed parallel to the z axis on the $-x$ surface of LN substrate. The central electrode width W_C is 8 μm; the electrode gaps G_C between the center and the two outer electrodes are also 8 μm. The length of electrodes L is 15 mm. A silicon dioxide buffer layer of 300 nm was deposited between the LN substrate and electrode layer. One of the outer electrodes V_2 is grounded ($V_2 = 0$ V), and two independent voltages V_C and V_1 can be applied to the center and the other outer electrodes, respectively. To characterize the phase-modulation and polarization-conversion characteristics under electrically driving voltages, the device was placed between a pair of parallel polarizer and analyzer (PL and AL). An incident He–Ne laser light of

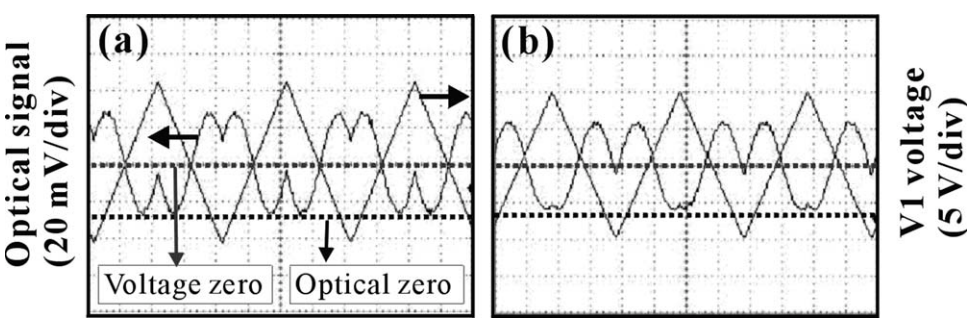

Figure 2 Measured response curves of the ZI phase modulators: (a) before and (b) after treatments

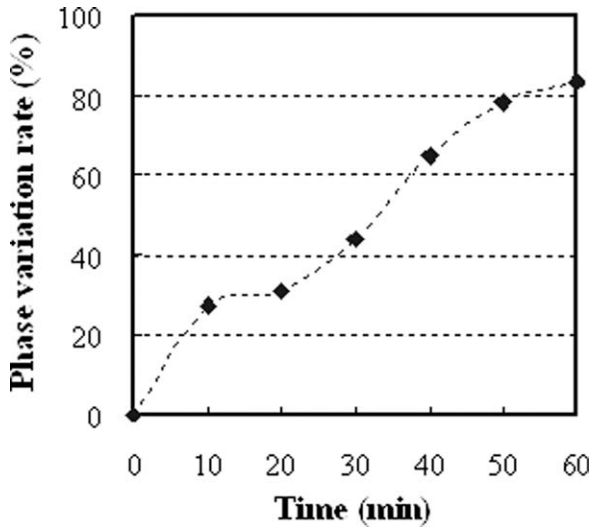

Figure 3 Phase variation rate as a function of time

633 nm wavelength was coupled into the polarization converter to be in the transverse magnetic (TM) polarization after passing through the PL and objective lens L1. The output light was focused with another lens L2. The throughput powers were measured behind a pinhole. After the AL, the signal is received by a photodetector. The normalized output power of TM polarization P_{TM} is represented as

$$P_{TM} = 1 - \frac{\kappa^2}{\kappa^2 + \delta^2} \sin^2\left(\sqrt{\kappa^2 + \delta^2} L\right), \tag{1}$$

where κ is the coupling coefficient, δ is the mismatch parameter between the transverse electric (TE) and TM modes [7]. These notations are further expressed by Eqs. (2) and (3).

$$\kappa = \left(\pi \Gamma_1 n_o^3 r_{61} / \lambda G_C\right) \cdot (V_C - V_1/2), \tag{2}$$

$$\delta = \Delta\beta/2 + \left(\pi \Gamma_2 n_o^3 r_{22} / \lambda (2G_C + W_C)\right) \cdot V_1, \tag{3}$$

where r_{61} and r_{22} are the EO coefficients, λ is the incident-light wavelength, and n_o is the ordinary refractive index of substrate. Γ_1 and Γ_2 are the overlap integrals for the vertical and horizontal electric fields between guided modes, respectively, $\Delta\beta$ is the modal birefringence. When the value of κ is much larger than that of δ and δ is near to zero, the complete polarization conversion is achievable at $\kappa L = \pi/2 \pm m\pi$ ($m = 0, 1, 2, \ldots$). The applied voltages and measured conversion curves can be obtained for calculating the overlap integrals of Γ_1 written as

$$\Gamma_1 = (\lambda G_C / n_o^3 r_{61}) \cdot (1/(V_{Cb} - V_{Ca})) \cdot (1/L), \tag{4}$$

where V_{Cb} and V_{Ca} are two adjacent V_C voltages to achieve the complete conversion under the same phase-matching voltage V_1. By floating the central electrode, the polarization converter is like a polarization-phase modulator to provide the phase-retardation modulation through the applied V_1 voltages. The normalized interferometric intensity P_{out} is expressed as

$$P_{out} = 1/2 + 1/2 \cdot \cos[\phi(t) + \pi V_1(t)/V_{1\pi}], \tag{5}$$

where $\phi(t)$ is a time-varying phase shift induced by the photorefractive effects. $V_1(t)$ is the applied triangular voltages. The corresponding interferometric signal can be measured to decide $V_{1\pi}$, which is the applied voltage for π phase retardation between the TE and TM modes. According to the measured $V_{1\pi}$, Γ_2 is given as

$$\Gamma_2 = (\lambda(2G_C + W_C)/2 n_o^3 r_{22} L V_{1\pi}). \tag{6}$$

3. RESULTS AND DISCUSSION

Through the focused modes of irradiating with a high power, the core region of the ZI waveguides can be heated due to the material absorptions. The induced temperature gradient enhances the diffusion abilities of free electrons. At the same time, the applied voltage provides a net electric force to make the electrons drift to the edge of waveguides. By using the treatments of biased voltage and laser trimming, we have observed the relations between the polarization-conversion stability and electron-depletion effects. The conversion performance of the same ZIPC was investigated before and after treatments. The proposed biased voltage and laser trimming were performed with a triangular voltage of AC peak-to-peak 20 V at a frequency of 100 Hz and a biased DC voltage of 10 V, under a throughput power of 30 μW and a long-term irradiation of 60 min at the incident light of 633 nm wavelength. The temporal changes of phase drifts induced by the photorefractive effects can be observed. Figure 2 presents the response curves of the phase modulator when measuring at a throughput power of 15 μW before and

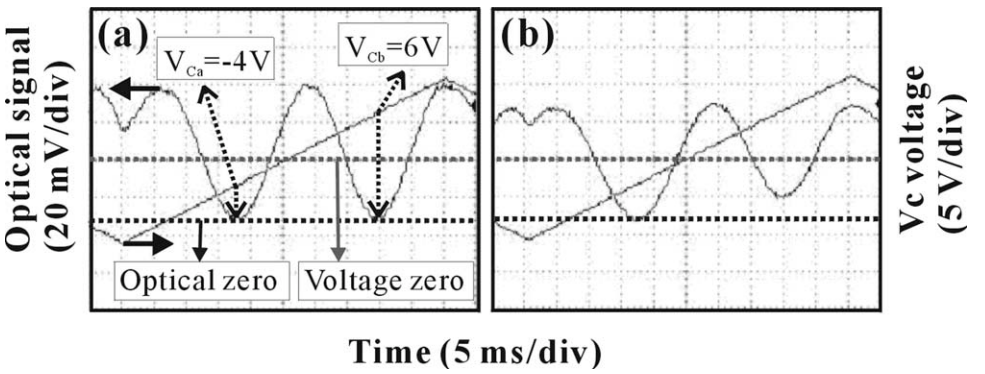

Figure 4 Polarization-conversion characteristics measuring at a throughput power of 25 μW before treatments: (a) initial measurement and (b) after 60 min

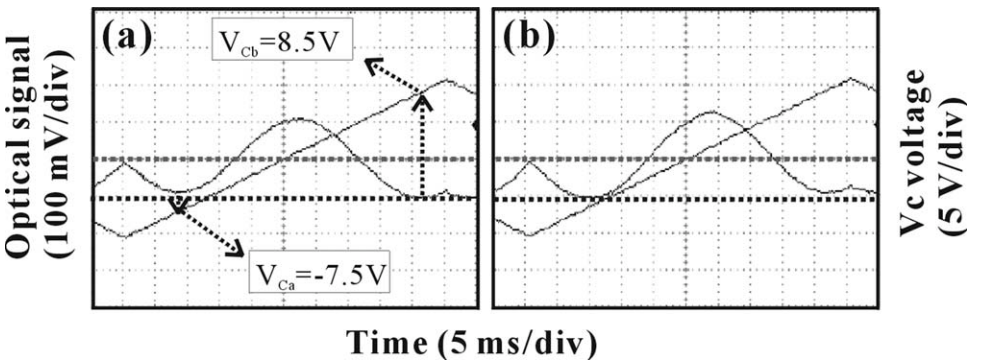

Figure 5 Polarization-conversion characteristics measuring at a throughput power of 80 μW after treatments: (a) initial measurement and (b) after 60 min

after treatments. The measurement results show that the values of $V_{1\pi}$ are the same, namely, about 11.5 V before and after treatments, as shown in Figure 2. However, the phase biases gradually changed during the observation period of 60 min. The phase variation rate is defined as a ratio of temporal phase-bias variations to the initial phase bias, as shown in Figure 3. This phenomenon was attributed to the time-varying space-charge field [$E_{sc}(t)$] forming due to the photorefractive effects. After long-term irradiating, the saturated phase drift implies that the waveguide region is depleted of the photoexcitable electrons. Figure 4 shows the conversion properties of the ZIPC before treatments. In the initial measurement, the applied voltages of $V_{Ca} = -4$ V and $V_{Cb} = 6$ V achieve complete conversion at the phase-matching voltage of $V_1 = 12$ V. However, the spatial distribution of photoexcitable electrons is dependent on the polarity of V_C voltages. In the case of $V_{Cb} > 0$, the horizontally nonuniform electrons induce the $E_{sc}(t)$ to compensate the optimized phase-matching voltages. It will cause an incomplete conversion

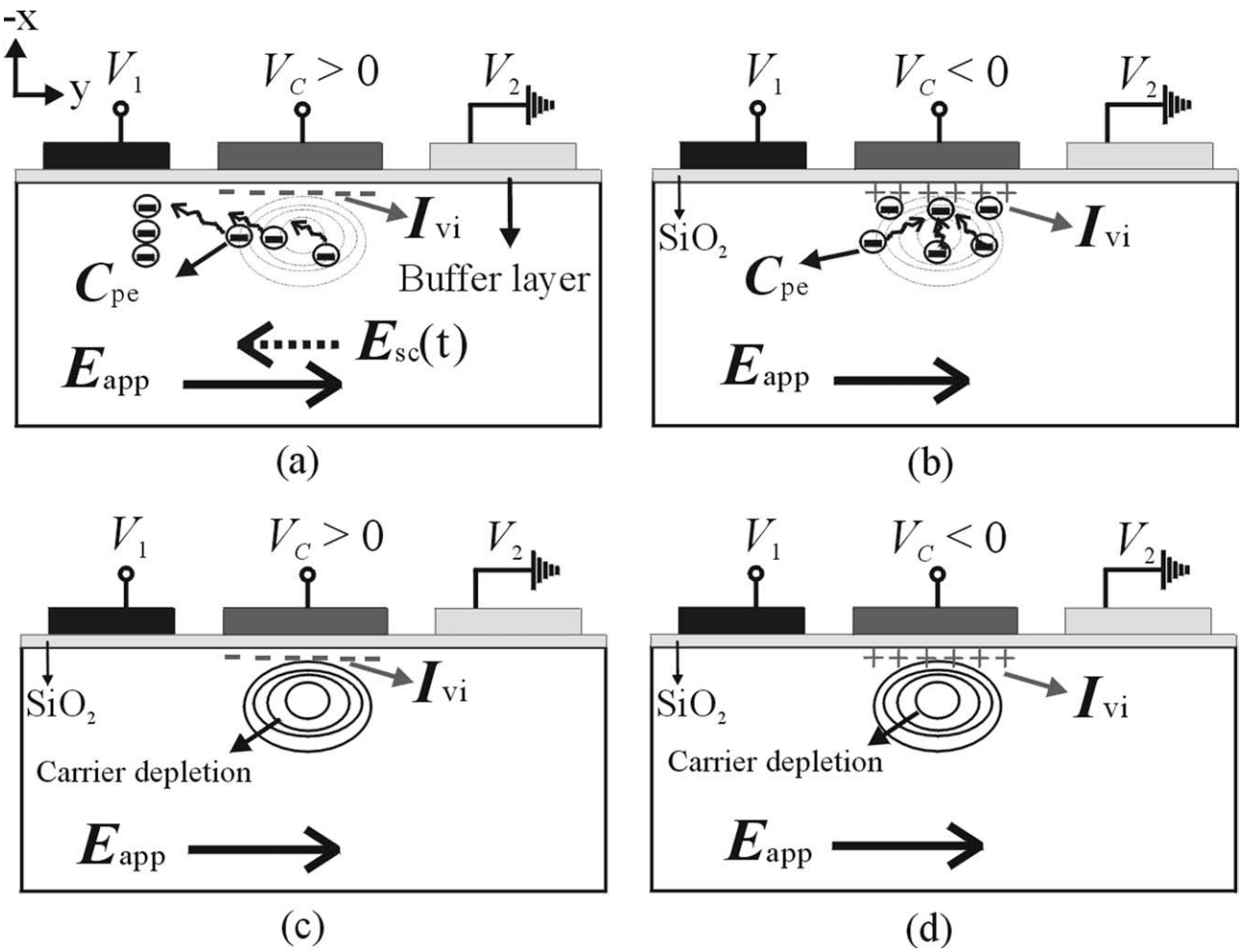

Figure 6 The schematic explanations of the electron-depletion effects on the stability improvements before and after treatments in different polarities of V_C voltages: (a) before treatments at $V_C > 0$, (b) before treatments at $V_C < 0$, (c) after treatments at $V_C > 0$, and (d) after treatments at $V_C < 0$

through an increase of time duration. After treatments, the phase-matching voltage of $V_1 = 12$ V is unchanged for a complete polarization conversion. Figure 5 shows the conversion results when measuring in the throughput powers of 80 μW with the same wavelength of 633 nm. In these measurements, the complete conversions from input TM polarization to TE one were achieved at the applied voltages of $V_{Ca} = -7.5$ V and $V_{Cb} = 8.5$ V. These values are higher than those before treatments (-4 and 6 V). However, the conversion properties are stable in both applied V_C voltages. Figure 6 gives the schematic explanations for the relations between depletion effects and conversion stabilities in different polarities of applied voltages V_C. Before the treatments, the distributions of photo-excited electrons (C_{pe}) are dependent on the voltage polarities. In the case of $V_C > 0$ as shown in Figure 6(a), the negatively voltage-induced ions (I_{vi}) are formed under the buffer layer, the repulsive force between the negative ions, and electrons will make the C_{pe} drifted slowly to the V_1 electrode side. The $E_{sc}(t)$ easily offsets the applied phase-matching electric field (E_{app}) and impacts the polarization-conversion stabilities. However, the positively I_{vi} are formed when applying voltage of $V_C < 0$ as shown in Figure 6(b), the C_{pe} will be trapped under the buffer layer. It do not induce the $E_{sc}(t)$ to change the phase-matching conditions. After the treatments, it is reasonable to expect that the waveguide region is depleted of the C_{pe} as shown in Figures 6(c) and 6(d). Therefore, the stable operations are independent on the polarity of applied V_C voltages, even irradiating with higher input powers again. The calculated values of Γ_1 are 0.4 and 0.25 measuring in before and after treatments, respectively. Before treatments, the measured TM mode size (full width at half maximum power intensity) was 2.8 μm (width) $\times$ 2.9 μm (depth).The mode size was changed to 3.2 $\times$ 3.7 μm^2 after treatments. Therefore, the higher voltages of V_C resulted from the smaller overlap integrals, probably due to a broader mode profile after treatments. The measured $V_{1\pi}$ and the corresponding Γ_2 are 11.5 V and 0.55, respectively, which are almost the same values before and after treatments. Because the gap width (24 μm) between the outside electrodes is wider than the guided mode width (3.2 μm), the horizontal overlap integrals are insensitive to the variations of mode size after treatments.

4. CONCLUSIONS

We have observed the relations between the carrier depletion effects and the improved stabilities of the ZIPC by using the treatments of biased voltage and laser trimming. Without the impacts from the time-varying space-charge electric field due to the photorefractive effects, the phase-matching conditions are stable. The long-term stabilities are achievable even when operating in a higher throughput power of 80 μW, compared with 25 μW before treatments at the incident light of 633 nm wavelength.

ACKNOWLEDGMENTS

This work was supported in part by the National Science Council of Taiwan (NSCT) under Grant NSC 95-2221-E-218-076.

REFERENCES

1. P. Gunter and J.-P. Huignard, Photorefractive materials and their applications, Springer, Berlin, 2006.
2. R.A. Becker, Thermal fixing of Ti-indiffused $LiNbO_3$ channel waveguides for reduced photorefractive susceptibility, Appl Phys Lett 45 (1984), 121–123.
3. B. Chen, J.F. Campos, W. Liang, Y. Wang, and C.Q. Xu, Wavelength and temperature dependence of photorefractive effect in quasi-phase-matched $LiNbO_3$ waveguides, Appl Phys Lett 89 (2006), 043510.
4. R.C. Twu, H.H. Lee, H.Y. Hong, and C.Y. Yang, A novel Zn-indiffused mode converter in x-cut lithium niobate, Opt Express 15 (2007), 15576–15582.
5. Y. Namihira and H. Wakabayashi, Real-time measurements of polarization fluctuations in an optical fiber submarine cable in a deep-sea trial using electrooptic $LiNbO_3$ device, IEEE J Lightwave Technol 7 (1989), 1201–1206.
6. F. Heismann, Compact electro-optic polarization scramblers for optically amplified lightwave system, IEEE J Lightwave Technol 14 (1996), 1801–1814.
7. T. Kawazoe, K. Satoh, I. Hayashi, and H. Mori, Fabrication of integrated-optic polarization controller using z-propagating Ti-$LiNbO_3$ waveguides, IEEE J Lightwave Technol 10 (1992), 51–56.
8. S. Thaniyavarn, Wavelength independent, optical damage immune z-propagation $LiNbO_3$ waveguide polarization converter, Appl Phys Lett 47 (1985), 674–677.
9. R.C. Twu, H.Y. Hong, and H.H. Lee, An optical homodyne technique to measure photorefractive-induced phase drifts in lithium niobate phase modulator, Opt Express 16 (2008), 4366–4374.
10. L. Ming, C.B.E. Gawith, K. Gallo, M.V. O'Connor, G.D. Emmerson, and P.G.R. Smith, High conversion efficiency single-pass second harmonic generation in a zinc-diffused periodically poled lithium niobate waveguide, Opt Express 13 (2005), 4862–4868.

SINGLE-WAVELENGTH FIBER LASER FOR LOCALIZED TEMPERATURE MONITORING

Zachary J. Chaboyer,[1] Jonas Valiunas,[1] Brian Adams,[2] Aicheng Chen,[2] and Gautam Das[1]
[1] Department of Physics, Lakehead University, Thunder Bay, Ontario P7B 5E1, Canada; Corresponding author: gdas@lakeheadu.ca
[2] Department of Chemistry, Lakehead University, Thunder Bay, Ontario P7B 5E1, Canada

Received 26 November 2009

ABSTRACT: *We report on a single-longitudinal-mode single-wavelength fiber laser and its applications for measuring localized temperature variation. The laser was developed using a fiber Bragg grating. The laser wavelength was single-longitudinal-mode with optical signal-to-noise ratio (OSNR) of more than 40 dB. The temperature sensitivity of the system was 11.08 pm/°C. To demonstrate the promising application of the laser sensor developed, we used the sensor to monitor the localized temperature of TiO_2 nanotubes during the photochemical process, and superparamagnetic iron oxides nanoparticles when exposed to low frequency magnetic field. The output of the laser was monitored using a scanning Fabry–Perot spectrum analyzer of resolution 6.7 MHz and an optical spectrum analyzer of resolution 3.75 GHz.* © 2010 Wiley Periodicals, Inc. Microwave Opt Technol Lett 52: 1941–1946, 2010; Published online in Wiley InterScience (www.interscience.wiley.com). DOI 10.1002/mop.25383

Key words: *fiber laser; single-mode fiber laser; saturable absorber; polarization-maintaining erbium-doped fiber; nanoparticles; temperature sensor; nanotubes*

1. INTRODUCTION

Fiber optic sensors based on fiber Bragg gratings (FBG) are already established as rugged, compact, cost effective, and reliable devices for practical applications. Many techniques have been